Please cite this article in press as: Schimek et al., High-fidelity predictions of diffusion in the brain microenvironment, Biophysical Journal (2024), https://doi.org/10.1016/j.bpj.2024.10.005

Biophysical Journal
Article

Biophysical Society

High-fidelity predictions of diffusion in the brain microenvironment

Nels Schimek,[1] Thomas R. Wood,[2] David A. C. Beck,[3,4,5] Michael McKenna,[5] Ali Toghani,[3] and Elizabeth Nance[4,5,6,*]

[1]Department of Chemistry, University of Washington, Seattle, Washington; [2]Department of Pediatrics, Division of Neonatology, University of Washington, Seattle, Washington; [3]Deparment of Computer Science and Engineering, University of Washington, Seattle, Washington; [4]eScience Institute, University of Washington, Seattle, Washington; [5]Department of Chemical Engineering, University of Washington, Seattle, Washington; and [6]Department of Bioengineering, University of Washington, Seattle, Washington

ABSTRACT Multiple-particle tracking (MPT) is a microscopy technique capable of simultaneously tracking hundreds to thousands of nanoparticles in a biological sample and has been used extensively to characterize biological microenvironments, including the brain extracellular space (ECS). Machine learning techniques have been applied to MPT data sets to predict the diffusion mode of nanoparticle trajectories as well as more complex biological variables, such as biological age. In this study, we develop a machine learning pipeline to predict and investigate changes to the brain ECS due to injury using supervised classification and feature importance calculations. We first validate the pipeline on three related but distinct MPT data sets from the living brain ECS—age differences, region differences, and enzymatic degradation of ECS structure. We predict three ages with 86% accuracy, three regions with 90% accuracy, and healthy versus enzyme-treated tissue with 69% accuracy. Since injury across groups is normally compared with traditional statistical approaches, we first used linear mixed effects models to compare features between healthy control conditions and injury induced by two different oxygen glucose deprivation exposure times. We then used machine learning to predict injury state using MPT features. We show that the pipeline predicts between the healthy control, 0.5 h OGD treatment, and 1.5 h OGD treatment with 59% accuracy in the cortex and 66% in the striatum, and identifies nonlinear relationships between trajectory features that were not evident from traditional linear models. Our work demonstrates that machine learning applied to MPT data is effective across multiple experimental conditions and can find unique biologically relevant features of nanoparticle diffusion.

SIGNIFICANCE Multiple particle tracking (MPT) is a microscopy technique that uses nanoparticle trajectory tracking to perform microrheological characterization of biological environments, including the vitreous of the eye, mucosal membranes, intracellular environments, and the brain extracellular space. MPT can generate gigabytes of data and is a prime candidate to benefit from advancements in machine learning and artificial intelligence to extract deeper insights. We present a robust and novel approach to control for correlation between related MPT trajectories to ensure the validity of predictions between healthy and diseased states of brain tissue. Our work demonstrates that machine learning applied to MPT data can predict biological variables with high accuracy across multiple biological systems and can identify biologically relevant subsets of features from nanoparticle diffusion data unique to each data set.

INTRODUCTION

The extracellular space (ECS) is a critical component of the brain that affects neurodevelopment (1), neuronal health (2,3), and transport of substances (4,5). Within the ECS is the brain extracellular matrix (ECM), a negatively charged scaffold-like structure made of proteoglycans and glycosaminoglycans (6–10). Specific components of the ECM play a crucial role in the maintenance of brain homeostasis including memory (11) and regulation of cellular processes (1). The structure and composition of the ECM not only differs temporally during development and aging (7), but also spatially, with known differences in structure (12) and protein expression (13) across brain regions.

Changes to the structure and composition of the ECS and ECM have been implicated in numerous disease conditions. For example, an increase in extracellular water as well as activity of proteins associated with ECM remodeling have

---

Submitted August 1, 2024, and accepted for publication October 8, 2024.

*Correspondence: eanance@uw.edu

Editor: Guy Genin.

https://doi.org/10.1016/j.bpj.2024.10.005

Please cite this article in press as: Schimek et al., High-fidelity predictions of diffusion in the brain microenvironment, Biophysical Journal (2024), https://doi.org/10.1016/j.bpj.2024.10.005

been connected to the pathophysiology of psychosis (14,15). Neurodegenerative diseases such as Parkinson's and Alzheimer's have shown altered parameters of diffusion in the ECS (16–20) and involvement of ECM components in pathological processes (21). Changes to fluid flow and expression of ECM components have been shown to occur in response to traumatic brain injury (22,23). Developing methods to detect changes in the brain microstructure can therefore be critical to understanding how pathological processes alter the brain ECS and the ECM.

Early studies that measured diffusion in the brain ECS to explore brain microstructure focused on two key parameters of ECS microstructure: volume fraction and tortuosity. Volume fraction is defined as the total volume of the ECS divided by the total volume of the entire brain tissue (24). Experiments using real-time iontophoresis of tetramethylammonium ions (TMA+) demonstrated that the ECS contributed to 20% of brain tissue volume (25). Tortuosity is calculated as the ratio between diffusivity in free medium compared the local ECS diffusivity (25), and measures the hindrance to diffusion caused by cellular obstruction and ECS connectivity (24). Both volume fraction and tortuosity vary during brain development (26); however, a critical finding by Kume-Kick et al. showed that there was a level of independence between the two parameters when ECS geometry changes (27). When the size of the ECS was altered by manipulation of NaCl content, the tortuosity increased as the volume fraction decreased, but when volume fraction increased the tortuosity value plateaued (27). Volume fraction and tortuosity have also been characterized across a number of disease and injury conditions (28–30), demonstrating that diffusion in the brain ECS can be used to detect changes in brain microstructure due to pathological conditions.

Advancements in the probes used for diffusion experiments have led to deeper understanding of the brain microstructure. Analysis of fluorescent dextran molecules revealed that dead space domains in the ECS exist in greater quantities when the rat neocortex becomes ischemic, leading to greater hindrance to diffusion due to increased tortuosity (31). In 2006, diffusion analysis of dextran molecules and quantum dots provided one of the first estimations of ECS pore sizes in living tissue, predicting the widths of pores to be between 38 and 64 nm (32). In 2012, diffusion of polystyrene-polyethylene glycol (PS-PEG)-coated nanoparticles revealed that 30% of pore widths in human brain tissue were greater than 110 nm with the largest having a width of 225 nm (33), a significant increase compared the previously reported value. The 2012 study showed that the surface functionalization of the probe influenced the probe's ability to diffuse, by taking the quantum dots used in the 2006 PNAS study and refunctionalizing them with a dense layer of PEG. These 2012 findings were later independently confirmed using single-walled carbon nanotubes, where the researchers demonstrated that pore sizes in the rodent neocortex can reach a width upward of 1 μm (34,35).

The recent success in tracking the diffusion of PS-PEG-coated nanoparticles and single-walled carbon nanotubes in the brain ECS highlights the potential for nanoparticle-based probes to uncover the nanoscale structure of the ECS, even with the use of two different tracking techniques: single-particle tracking (SPT) and multiple-particle tracking (MPT). SPT and MPT are both microscopy techniques capable of measuring diffusion in living tissue. Both methods track fluorescently labeled nanoparticles that are introduced into the biological system of interest. A key difference between SPT and MPT is the length and number of trajectories collected for each technique. For SPT, there are a low number of trajectories collected but they can be tracked for several to tens of minutes (36). SPT methods have been used extensively to assess the organization of the brain ECS (34,35,37), detect pathological changes (38), and determine local rheological properties (34). MPT tracks trajectories at much short time lengths but collects hundreds to thousands of trajectories for a given video. MPT has enabled the study of ECS structure such as the distribution of pore sizes (33) and the effect of surface coating on nanoparticle diffusion (33), changes to diffusion due to ischemic brain injury (39,40), changes to the ECM during development (41), and enzymatic degradation of the ECM (41).

Both SPT and MPT present opportunities for the use of machine learning (ML) due to the high dimensionality of data generated. For SPT, the high dimensionality of the data is not the number of trajectories, but the length of trajectories. The long length and timescale of diffusing particles captured by SPT has led to accurate predictions of diffusion modes from interpretable models such as linear discriminant analysis, random forests, and gradient boosted decision trees (42–46), and most prominently by using neural networks (45–55). Due to the number of nanoparticles that can be tracked during MPT experiments, ML models can be trained directly on trajectories tracked in biological environments. For example, artificial neural networks were trained on MPT and accurately predicted nanoparticle size, surface functionality, stiffness, and viscosity based on nanoparticle behavior in hydrogels and rodent ex vivo brain slices (56). Neurodevelopmental age of rodent ex vivo brain slices was then predicted using a gradient boosted decision tree model (41) trained on trajectories from MPT videos captured in rodent ex vivo brain slices. Both studies demonstrate that ML can be used to detect changes in MPT data that relate to the microenvironment of the ECS.

Driven by these earlier studies using ML, more work is needed to ensure that additional complex biological variables can be accurately predicted using MPT data, and that further optimization of the tools and methods can glean insightful information from these robust data sets. Whereas MPT has previously been used to characterize changes in diffusion as a result of an induced disease condition (39),

Please cite this article in press as: Schimek et al., High-fidelity predictions of diffusion in the brain microenvironment, Biophysical Journal (2024), https://doi.org/10.1016/j.bpj.2024.10.005

it is unknown whether a ML algorithm can accurately distinguish between healthy and diseased tissue states based on MPT data. In addition, aside from the diffusion coefficient, which has been shown to change because of a disease condition, it is not known whether other features of nanoparticle trajectories are different between a healthy and diseased state.

To address these questions, we develop and validate an explainable ML pipeline to predict changes to the ECS due to age differences, regional differences, and enzymatic degradation. We then use the pipeline to predict between healthy tissue and two disease states in two different regions and determine subsets of predictive features. By applying explainable ML to multiple different systems, we determine whether supervised ML models can learn unique nonlinear relationships between features for different biological states that are not identified by traditional linear statistics.

MATERIALS AND METHODS

Data acquisition

All data utilized in this study exist in published databases as described in the results. No animal studies were performed in this study; however, all published data collected were performed in animal studies in strict accordance with the recommendations in the Guide for the Care and Use of Laboratory Animals of the National Institutes of Health (NIH). All animals were handled according to approved institutional animal care and use committee (IACUC) protocols (no. 4383-02) of the University of Washington. The University of Washington has an approved Animal Welfare Assurance (no. A3464-01) on file with the NIH Office of Laboratory Animal Welfare (OLAW), is registered with the United States Department of Agriculture (USDA, certificate no. 91-R-0001), and is accredited by AAALAC International. OWH brain slices were prepared from male Sprague-Dawley rat pups (Charles River, Wilmington, MA) at varying ages for the age data set (41) and at postnatal day 10 (P10) for all other data sets.

After euthanasia, brains were extracted, immersed in room temperature (22°C) dissection medium, and cut into hemispheres with a razor blade. Coronal slices (300 μm thick) were prepared from each hemisphere using a McIlwain tissue chopper (Ted Pella, Redding, CA) (40). Individual OWH slices were plated on 30 mm cell culture inserts (MilliporeSigma, Burlington, MA) in nontreated 6-well plates (USA Scientific, Ocala, FL) filled with 1 mL slice culture medium and incubated in sterile conditions at 37°C and 5% CO_2. For OWH slices obtained from P14, P35, and P70 pups for the age data set, MPT was preformed within 6 h (acute) after slice explantation. For OWH slices from P10 rats to assess regional differences in diffusion, slices were cultured for 4 days in vitro (DIV) before MPT. For OWH slices exposed to enzymes, slices were obtained from P35 rats and immediately after explantation were treated with either chondroitinase ABC (ChABC) for 120 min before MPT (41). For oxygen glucose deprivation (OGD) (57) exposure in OWH slices, OGD medium was made by adding 120 mM sodium chloride (NaCl, MilliporeSigma), 2.8 mM potassium chloride (KCl, Sigma), 1 mM calcium chloride ($CaCl_2$, MilliporeSigma), and 10 mM 4-(2-hydroxyethyl)piperazine-1-ethanesulfonic acid buffer solution (HEPES, Gibco, Waltham, MA) to deionized water, which was then titrated using 1 M hydrochloric acid (Thermo Fisher Scientific, Waltham, MA) or 1 M sodium hydroxide (Thermo Fisher Scientific) to a pH of 7.4. The medium was then bubbled with nitrogen gas (Praxair, Danbury, CT) for 10 min. OGD was performed by adding 1 mL OGD medium to OWH samples, which were then incubated at 37°C while in a nitrogen-purged Hypoxia Incubator Chamber (STEMCELL Technologies, Vancouver, British Columbia, Canada) for 0.5 or 1.5 h. At the end of OGD exposure, OGD medium was removed and slices were returned to normal slice culture medium and 5% CO_2 conditions at 37°C.

For MPT analysis for all studies, nanoparticle probes were applied topically to slices and incubated for 30 min before imaging. Nanoparticle probes were 40 nm fluorescent carboxylate (COOH)-modified PS nanoparticles (PS-COOH) (Fisher Scientific, Hampton, NH) covalently modified with methoxy (MeO)-PEG-amine (NH_2) (5 kDa MW, Creative PEG Works, Winston-Salem, NC) by carboxyl amine reaction (58). The MPT videos used in this study were collected through fluorescent microscopy using a CMOS camera (Hamamatsu Photonics, Hamamatsu City, Japan) mounted on a confocal microscope. Each MPT video was collected using a frame rate of 33.3 frames per second for 651 frames at 100× magnification (oil immersion, 1.45 numerical aperture, Nikon, Melville, NY).

Statistical analysis

To compare individual MPT features between different OGD groups, linear mixed effects models were performed using the lme4 software package in R (59,60). A model was fit for each locally averaged feature for each individual MPT trajectory to determine fixed effects of the OGD group using the healthy control (HC) condition as the reference group. Each model included random effects of both slice and MPT video to account for correlation between individual MPT trajectories taken from the same slice as well as trajectories from particles whose data were collected in the same video at the same time. When comparing across multiple groups, differences were compared using linear combinations derived from the emmeans package, and p values < 0.05 were defined as statistically significant.

eXtreme Gradient Boosting

XGBoost (eXtreme Gradient Boosting) is a ML software package that uses boosted decision trees for its models (61). A boosted decision tree model is built by sequentially adding weak prediction models fit to a subset of the full data set, continuing until a specific number of weak models is reached or the loss function of the model converges. Final predictions of the model are made through a weighted average of the predictions of each of the weak learners (62). XGBoost was chosen, as tree-based models, including XGBoost, have been shown to be successful at ML tasks related to particle tracking predictions both for classification accuracy, as well as interpreting which statistical features of MPT data contributed the most to predictions (41,43,44).

Shapley additive explanations

Shapley additive explanation (SHAP) values were calculated for each statistical feature in each of the data sets to determine the contribution of each feature to model predictions across each data set (63). SHAP values originate from the game theory approach of Shapley values, and are calculated for each feature by averaging how much that feature contributes to each prediction instance (63). Calculating SHAP values for MPT data is useful as each of the 33 features used to train the model captures a unique aspect of the data. Determining which subsets of features are most important for different MPT data sets can inform which aspects of nanoparticle trajectory diffusion are being impacted by the microenvironment they experience.

XGBoost predictions

The XGBoost software package generated classification predictions on each of the four data sets. Data were cleaned by removing trajectories that had missing or infinite values for any of the features. To prevent overfitting, data sets were rebalanced through majority class under sampling to ensure that each class had the same number of data points. To ensure that there was no data leakage between the training and testing data, trajectories

Please cite this article in press as: Schimek et al., High-fidelity predictions of diffusion in the brain microenvironment, Biophysical Journal (2024), https://doi.org/10.1016/j.bpj.2024.10.005

TABLE 1 XGBoost metrics for each class in the age data set, and for the overall model, reported as median and interquartile range from 50 models trained on random, downsampled subsets of data

Evaluation	P14	P35	P70	Total
Normal model				
Accuracy	0.88 ± 0.02	0.80 ± 0.03	0.90 ± 0.04	0.86 ± 0.02
Precision	0.91 ± 0.03	0.79 ± 0.03	0.89 ± 0.02	0.86 ± 0.01
Recall	0.88 ± 0.02	0.80 ± 0.03	0.90 ± 0.04	0.86 ± 0.01
F1 score	0.89 ± 0.02	0.80 ± 0.03	0.89 ± 0.02	0.86 ± 0.02
Y-scrambled model				
Accuracy	0.34 ± 0.02	0.34 ± 0.04	0.33 ± 0.02	0.34 ± 0.01
Precision	0.33 ± 0.02	0.34 ± 0.02	0.34 ± 0.02	0.34 ± 0.01
Recall	0.34 ± 0.02	0.34 ± 0.02	0.33 ± 0.02	0.34 ± 0.01
F1 score	0.34 ± 0.02	0.34 ± 0.02	0.34 ± 0.02	0.34 ± 0.01

from the same local environment were binned together such that, when split for training and testing, trajectories from the same bin were only in the training set or test set, never both. Training and testing data sets were chosen by randomly assigning bins to each such that the split is 80:20. During model training, 10% of the training data were used for internal validation, which left a total of 70% of the class balanced data set for training.

Feature data consisted of the statistical features (Table S1) generated with *diff_classifier*, and the target variable was either age, region, or treatment type. A cross-validation hyperparameter search was used to determine the optimal hyperparameters of an XGBoost model for each of the different data sets (Table S2). SHAP values were used to determine the importance of each feature to the model's predictive ability. Y-scrambling, where the target variables were randomly reassigned for each feature row, was used in conjunction with XGBoost to determine the likelihood of chance predictions.

RESULTS

Data collection

For this study, we developed an explainable ML pipeline capable of predicting between injury states based on nanoparticle diffusion. We used linear effects modeling to compare features of MPT data between conditions in the injury model. Before predicting between injury states, we validated the pipeline on three sets of MPT data collected from distinct biological conditions in OWH slices—nanoparticles tracked in the cortex at different brain ages, nanoparticles tracked in different brain regions at the same age, and nanoparticles tracked in the HC or in enzymatically degraded ECM conditions in the cortex. We then applied the linear mixed models and the explainable ML pipeline to MPT data from an OGD injury model in OWH slices.

Nanoparticle diffusion data were previously obtained using MPT in rat 300 μm OWH thick brain slices from three independent experiments. Although no new raw data were generated in this article, the experimental methods that produced the data sets are briefly described in the materials and methods. In the first experiment, age-dependent diffusion data were acquired from OWH slices collected from the cortex of male pups at P14, P35, and P70 (41), defined as the age data set. In the second experiment, brain region-dependent diffusion data were acquired from OWH brain slices from P10 male pups that included the cortex, striatum, and hippocampus, defined as the region data set. The third experimental data set contains diffusion data from P35 male pup brain slices exposed to enzymatic degradation of ECM structures using ChABC and HC slices, defined as the treatment data set (41). The fourth experimental data were from P10 male pup slices from the striatum or cortex from HC slices, slices treated with 0.5 h OGD (57) or 1.5 h OGD treatment (39). Data from OGD-treated slices were chosen due to it being a well-characterized disease state, where OGD increases cell death and cell proliferation regionally and temporally (40), reduces glutathione production (39), drives changes to the morphology of microglia (39,64), and increases proinflammatory and oxidative stress markers (39,64). From the acquired diffusion data, we generated statistical features for each nanoparticle trajectory with the open-sourced *diff_classifier* package (65). A list and description of the features is provided in Table S1.

XGBoost accurately predicts complex biological variables across multiple data sets

To establish the likelihood of correct predictions occurring by chance, XGBoost models were trained on Y-scrambled data for each data set and had accuracy scores close to that of random guessing for the age data set (Table 1), the region data set (Table 2), and the treatment data set (Table 3). Precision, recall, and F1 score metrics of the Y-scrambled models show the lack of any predictive capacity for these models. Predictions on the age data set (Table 1) and region data set (Table 2) with the normal XGBoost model are higher than predictions with the Y-scrambled XGBoost model (+0.52 and +0.56, respectively). Predictions using normal XGBoost of the treatment data set (Table 3) were also higher by +0.19 compared with the Y-scrambled XGBoost model. A confusion matrix of a model trained on all five regions showed that trajectories from the thalamus were almost equally likely to be predicted as hippocampus as they were thalamus, which is one possible reason that interchanging hippocampus for thalamus led to similar model accuracy. The hippocampus was chosen over the thalamus for the final model because it was predicted correctly at a higher rate when a model was trained on all five regions.

SHAP shows mean diffusion as most important feature

A significant benefit of using a boosted decision tree model on MPT data is that, in addition to seeing whether a model can predict complex biological variables, feature importance methods can be used to determine which features were used to generate predictions and learn patterns in the

Please cite this article in press as: Schimek et al., High-fidelity predictions of diffusion in the brain microenvironment, Biophysical Journal (2024), https://doi.org/10.1016/j.bpj.2024.10.005

TABLE 2 XGBoost metrics for each class in the region data set, and for the overall model, reported as median and interquartile range from 50 models trained on random, downsampled subsets of data

Evaluation	Cortex	Hippocampus	Striatum	Total
Normal model				
Accuracy	0.88 ± 0.08	0.96 ± 0.01	0.86 ± 0.02	0.90 ± 0.03
Precision	0.85 ± 0.04	0.98 ± 0.01	0.86 ± 0.04	0.90 ± 0.03
Recall	0.88 ± 0.08	0.96 ± 0.01	0.86 ± 0.02	0.90 ± 0.03
F1 score	0.86 ± 0.06	0.97 ± 0.01	0.86 ± 0.02	0.90 ± 0.03
Y-scrambled model				
Accuracy	0.34 ± 0.02	0.33 ± 0.02	0.33 ± 0.02	0.34 ± 0.01
Precision	0.33 ± 0.02	0.34 ± 0.02	0.33 ± 0.02	0.34 ± 0.01
Recall	0.33 ± 0.02	0.34 ± 0.02	0.34 ± 0.02	0.34 ± 0.01
F1 score	0.34 ± 0.02	0.33 ± 0.02	0.34 ± 0.02	0.34 ± 0.01

TABLE 3 XGBoost metrics for each class in the treatment data set, and for the overall model, reported as median and interquartile range from 50 models trained on random, downsampled subsets of data

Evaluation	ChABC treated	Nontreated	Total
Normal model			
Accuracy	0.66 ± 0.02	0.72 ± 0.03	0.69 ± 0.02
Precision	0.70 ± 0.03	0.68 ± 0.02	0.69 ± 0.02
Recall	0.67 ± 0.02	0.72 ± 0.03	0.69 ± 0.02
F1 score	0.69 ± 0.02	0.70 ± 0.02	0.69 ± 0.02
Y-srambled model			
Accuracy	0.48 ± 0.01	0.52 ± 0.03	0.50 ± 0.01
Precision	0.50 ± 0.01	0.50 ± 0.01	0.50 ± 0.01
Recall	0.48 ± 0.01	0.52 ± 0.03	0.50 ± 0.01
F1 score	0.49 ± 0.01	0.51 ± 0.02	0.50 ± 0.01

data. By finding the most important features in an MPT data set, it is possible to gain insight into how the trajectories differ between independent classes. We can begin to understand the biological and chemical differences that led to the model being able to generate predictions much higher than random guessing.

SHAP feature importance from an XGBoost model trained on the age data set showed that the mean diffusion coefficient at 0.33 s (mean Deff1) was the most important feature, with a magnitude of 2.4 (Fig. 1 *A*). That magnitude was more than double that of the second most important feature, the mean fitted anomalous diffusion coefficient (mean D_fit), which had a magnitude of 1.1. Four other features had a magnitude above 0.5: mean boundedness, mean trappedness, mean straightness, and mean fractal_dim. The top 12 features were all locally average mean features, demonstrating the value that local averaging of the trajectory data adds to predictive capacity. These magnitude values were all much higher than the SHAP values determined for the Y-scrambled XGBoost model (Fig. 1 *B*). In the Y-scrambled model the top feature, kurtosis, had a magnitude of 0.086, only greater than the 15th ranked feature by 0.026. The low-magnitude SHAP values and similarity in magnitude across the top 15 features indicates that the high magnitudes found in the normal XGBoost model are representative of key components of the data that differentiate trajectories from different age groups.

Similar to the results from the age data set, the top feature for the region data set was mean Deff1with a magnitude of 2.3 (Fig. 1 *C*). Mean fractal_dim was the only other feature above 1.0 with a magnitude of 1.3 and mean Deff2 (mean diffusion coefficient at 3.3 s), mean D_fit, and mean kurtosis were all above 0.5, indicating the key features driving differentiation between trajectory motion in the different regions. SHAP values of an XGBoost model trained on Y-scrambled data showed features with magnitudes all below 0.04 (Fig. 1 *D*), demonstrating the lack of predictive power from the Y-scrambled features.

SHAP feature importance for an XGBoost model trained on the treatment data showed much lower magnitudes compared with the age and region data sets (Fig. 1 *E*), which was unsurprising due to the comparatively lower prediction accuracies on the treatment data set. Mean Deff1 was again the top feature but had a magnitude of only 0.55. Mean D_fit, with a magnitude of 0.12, was the only other feature with a magnitude above 0.1. SHAP values from an XGBoost model trained on Y-scrambled data from the treatment data set all fell below 0.015 (Fig. 1 *F*), again showing no predictive power from the Y-scrambled data. The low magnitudes of the SHAP values from the normal XGBoost model on the treatment data set indicate that mean Deff1 was the only feature the model could consistently use to differentiate between trajectories from the two classes. Despite the low magnitude, the even lower SHAP values of the Y-scrambled model indicate there are true differences in the diffusion coefficients of trajectories from HC and ChABC-treated slices that can be identified by the XGBoost model.

SHAP captures statistically significant features across age

To validate that the most important features determine by SHAP were indicative of regional and neurodevelopmental differences, a linear mixed effects model was used to determine whether features differed between age groups and brain regions when accounting for potential random effects due to slice variability. Three of the top 6 most important features—mean Deff1, mean straightness, and mean D_fit—followed the same trend, where the mean value of the feature was highest in the P14 group and decreased in each of the P35 and P70 groups (Fig. 2, *A–C*), with each age group being statistically significant from each other for each feature. For mean Deff1, the mean value was 22.84 for P14 (95% confidence interval of [19.94, 25.74]), which decreased to 7.56 ([4.66, 10.45], $p < 0.001$) for P35 and was lowest for P70 at 2.20

Please cite this article in press as: Schimek et al., High-fidelity predictions of diffusion in the brain microenvironment, Biophysical Journal (2024), https://doi.org/10.1016/j.bpj.2024.10.005

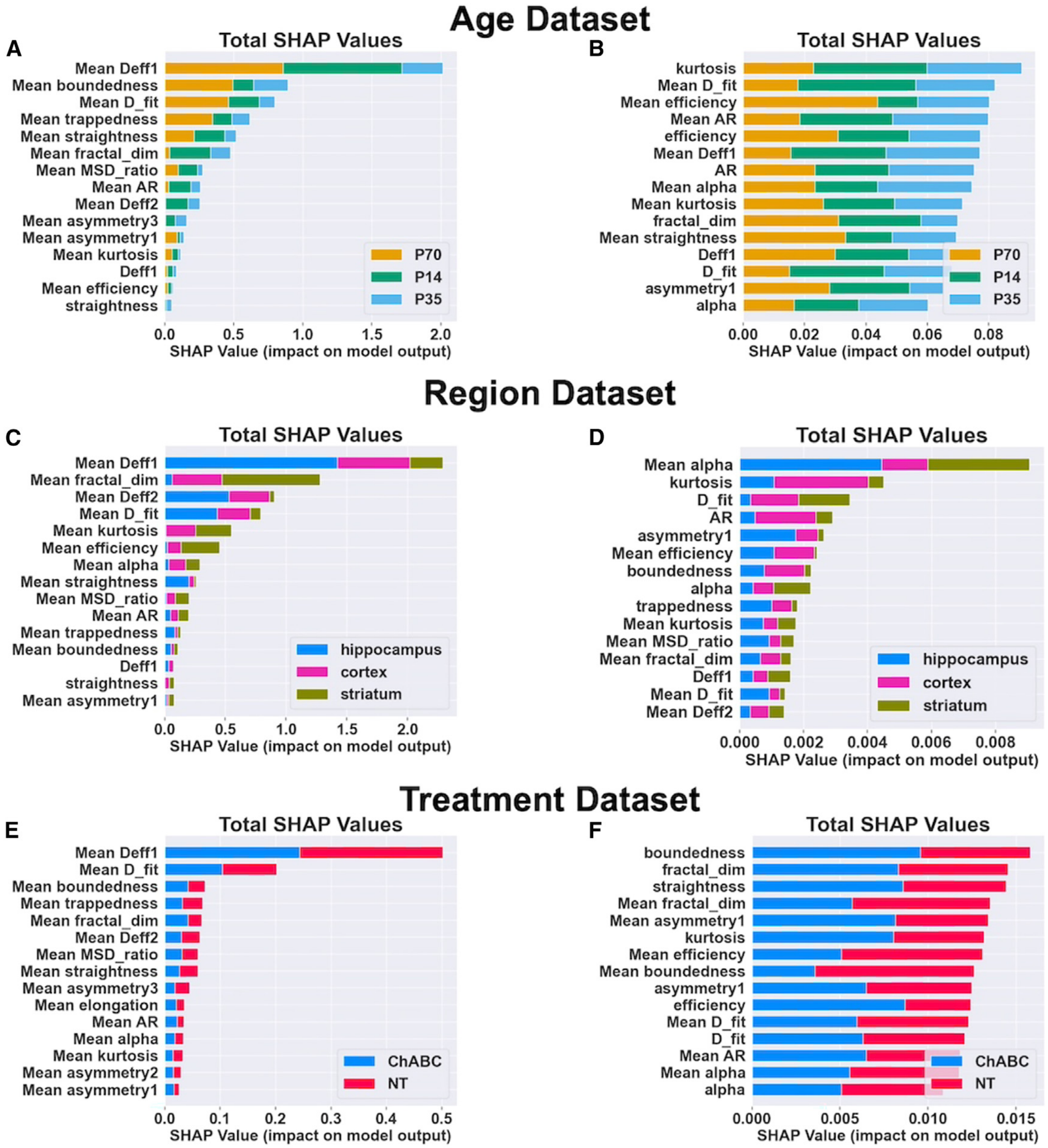

FIGURE 1 SHAP values of normal and Y-scrambled models for each data set. (*A*) Ranked SHAP features for XGBoost model trained on age data set with all features. (*B*) Ranked SHAP features for XGBoost model trained on Y-scrambled age data set with all features. (*C*) Ranked SHAP features for XGBoost model trained on region data set with all features. (*D*) Ranked SHAP features for XGBoost model trained on Y-scrambled region data set with all features. (*E*) Ranked SHAP features for XGBoost model trained on enzyme-treated data set with all features. (*F*) Ranked SHAP features for XGBoost model trained on Y-scrambled enzyme-treated data set with all features.

([−0.733, 5.12], $p < 0.001$ compared with P14 and $p < 0.05$ compared with P35) (Fig. 2 *A*). The mean value at P14 for mean straightness was 0.34 ([0.317, 0.364]), 0.217 ([0194, 0.241], $p < 0.001$ compared with P14) at P35, and 0.146 ([0.122, 0.170], $p < 0.001$ compared with both P14 and P35) at P70 (Fig. 2 *B*). Mean D_fit had a mean value of 29.52 ([26.24, 32.8]) at P14, which decreased to 17.19 ([13.93, 20.5], $p < 0.01$ compared with P14) at P35 and 6.48 ([3.15, 9.8], $p < 0.001$ compared with both P14 and P35) at P70 (Fig. 2 *C*). Mean trappedness and mean boundedness followed similar trends where there P14 and P35 did not differ significantly, while P70 was lower compared with both other ages (Fig. 2, *D* and *E*). For mean trappedness, the mean values for P14 and P35 were both −0.194 ([−0.193, −0.195]) while the mean value for P70 was −0.204 ([−0.203, −0.205], $p < 0.001$ compared with both P14 and P35). For P14 and P35, the mean values of mean boundedness were 0.110 ([0.107, 0.114]) and 0.109 ([0.106, 0.133]), respectively, decreasing to 0.0758 ([0.072, 0.080], $p < 0.001$

Please cite this article in press as: Schimek et al., High-fidelity predictions of diffusion in the brain microenvironment, Biophysical Journal (2024), https://doi.org/10.1016/j.bpj.2024.10.005

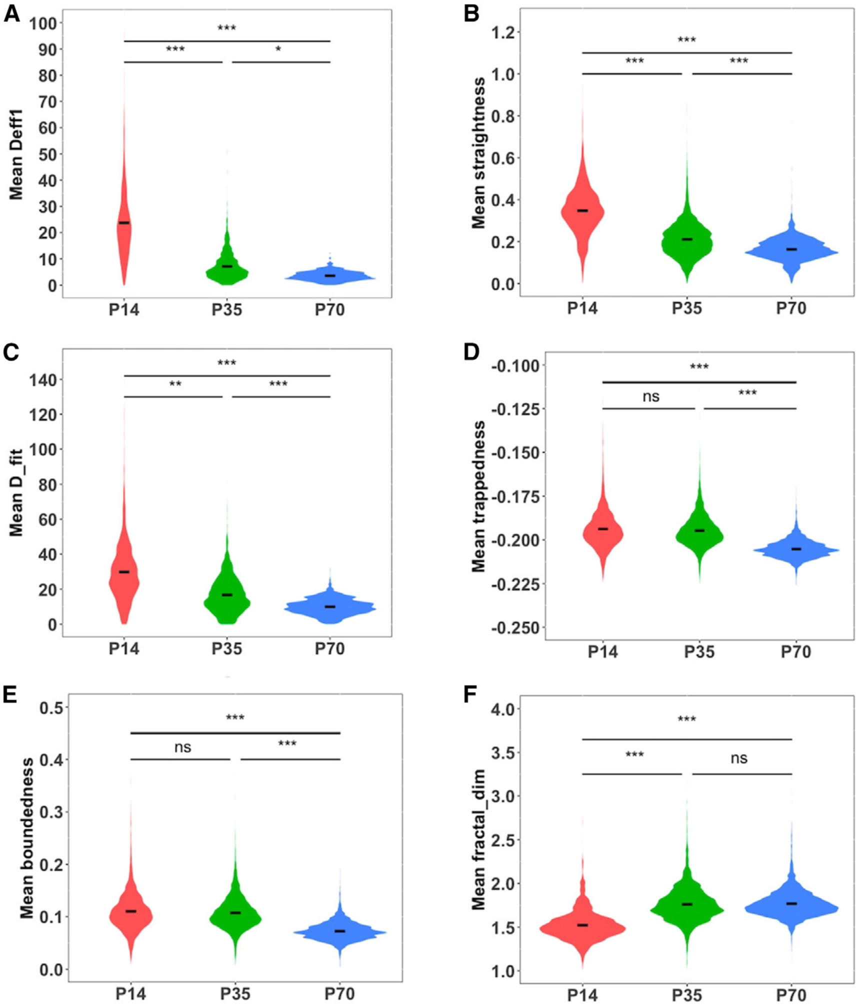

FIGURE 2 Distributions of statistically significant features for age data set when accounting for fixed effects. (*A*) Violin plots showing the distributions of the mean Deff1 feature for each age. (*B*) Violin plots showing the distribution of the mean straightness feature for each age. (*C*) Violin plots showing the distributions of the mean Deff1 feature for each age. (*D*) Violin plots showing the distribution of the mean straightness feature for each age. (*E*) Violin plots showing the distributions of the mean Deff1 feature for each age. (*F*) Violin plots showing the distribution of the mean straightness feature for each age. Statistical significance is indicated by $*p < 0.05$, $**p < 0.01$, $***p < 0.001$.

compared with both P14 and P35) for the P70 group. Mean fractal_dim was lowest in the P14 group with a value of 1.53 ([1.48, 1.59]) and was significantly different compared with both P35 at 1.75 ([1.70, 1.81], $p < 0.001$) and P70 and 1.81 ([1.75, 1.87], $p < 0.001$) (Fig. 2 *F*). Mean fractal dimension was not significantly different between the P35 and P70 groups.

The most important SHAP features for the region data set also captured regional differences that were found to be statistically significant. Mean Deff1, mean D_fit, and mean efficiency showed similar trends where all regions where comparisons between all regions showed statistically significant differences with data the value from the hippocampus being the highest across each feature. Mean Deff1 was lowest in the striatum with a mean value of 0.66 ([0.34, 0.97], $p < 0.001$), slightly higher in the cortex at 0.81 ([0.49, 0.1.12], $p < 0.001$), and had a value of 11.55 ([11.23, 11.87], $p < 0.001$) in the hippocampus (Fig. 3 *A*). The mean value of mean D_fit was lowest in the cortex at 1.69 ([−0.322, 3.7], $p < 0.001$), increased in the striatum at 2.49 ([0.49, 4.5], $p < 0.001$) and was 16.44 ([14.43, 18.40], $p < 0.001$) in the hippocampus (Fig. 3 *B*). Mean efficiency was lowest in the striatum at 0.26 ([0.14, 0.39, $p < 0.001$]), with a value of 0.44 ([0.31, 0.56], $p < 0.001$) in the cortex and 1.02 ([0.89, 1.14], $p < 0.001$) in the hippocampus (Fig. 3 *C*). Mean values for mean kurtosis and mean fractal_dim differed across each region with each feature following similar trends. Mean kurtosis was lowest in the hippocampus at 3.32 ([2.22, 4.42], $p < 0.001$), increased to 4.10 ([3.00, 5.20], $p < 0.001$) in the cortex, and was highest in the striatum at 4.55 ([3.45, 0.32], $p < 0.001$) (Fig. 3 *D*). Similarly, mean fractal_dim had a value of 1.80 ([1.36, 2.25], $p < 0.001$) in the hippocampus, 2.18 ([1.74, 2.63], $p < 0.001$) in the cortex, and was 2.31 ([1.87, 2.76], $p < 0.001$) in the striatum (Fig. 3 *E*). Mean Deff2 was found to be not significant between the cortex and striatum with mean values of 0.141 (−0.03, 0.31) and 0.143 ([−0.03, 0.32]), respectively, while the value of mean Deff2 hippocampus was significantly different

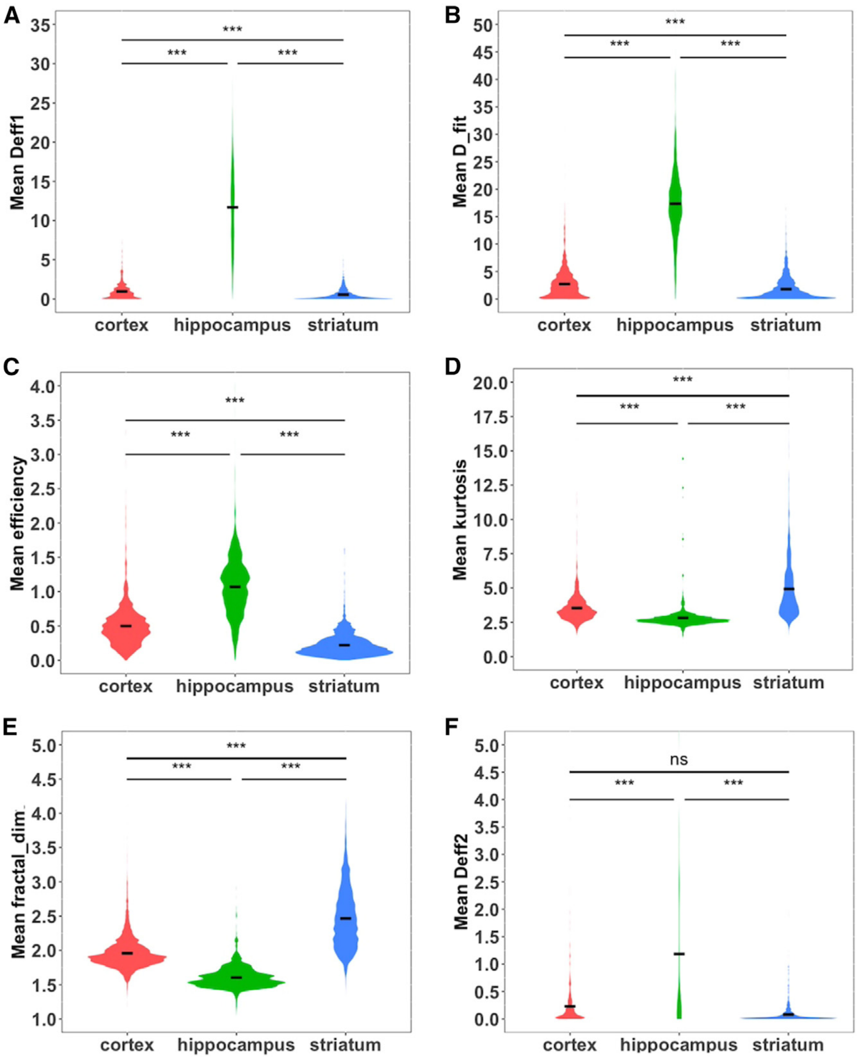

FIGURE 3 Distributions of statistically significant features for region data set when accounting for fixed effects. (*A*) Violin plots showing the distributions of the mean Deff1 feature for each region. (*B*) Violin plots showing the distribution of the mean D_fit feature for each region. (*C*) Violin plots showing the distributions of the mean efficiency feature for each region. (*D*) Violin plots showing the distribution of the mean kurtosis feature for each region. (*E*) Violin plots showing the distributions of the mean fractal_dim feature for each region. (*F*) Violin plots showing the distribution of the mean Deff2 feature for each region. Statistical significance is indicated by $^{*}p < 0.05$, $^{**}p < 0.01$, $^{***}p < 0.001$.

compared with both cortex and striatum at 1.098 ([0.92, 1.27], $p < 0.001$) (Fig. 3 *F*).

Distribution of geometric features shows differences between healthy and disease conditions

To decrease model complexity and increase interpretability, we used a decreased number of features published in previous literature (43). The features fall under three primary categories: those related to the MSD data (Deff1 and mean Deff1, MSD_ratio mean MSD_ratio, alpha and mean alpha, trappedness and mean trappedness), those related to the radius of gyration tensor (kurtosis and mean kurtosis, asymemetry1, and mean asymmetry1), and those related to the steps in a trajectory (fractal_dim and mean fractal_dim, straightness and mean straightness, efficiency and mean efficiency). To determine any effects due to brain slice variability and trajectory length, we used a linear mixed effects model and assessed whether the mean of each locally averaged feature was significantly different between the HC data and each treatment condition while accounting for slice effects and trajectory length effects. Correlation plots between each feature and trajectory length are shown in Fig. S1, where there was not a common directionality of effect of the trajectory length on individual features. For the cortex data, mean MSD_ratio feature was significant for the 0.5 and 1.5 h OGD conditions when accounting for slice effects, while mean fractal_dim was significant for the 0.5 h OGD condition. The mean of the mean MSD_ratio feature was 0.88 for the HC, which decreased to 0.60 (95% confidence interval of [0.528, 0.672], $p = 0.037$) in the 0.5 h OGD condition and to 0.633 ([0.561, 0.706], $p = 0.037$) in the 1.5 h OGD condition (Fig. 4 *A*). The mean of the mean fractal_dim feature was 1.98 in the HC condition, decreasing to 1.74 (95% confidence interval of [1.63, 1.82], $p = 0.041$) in the 0.5 h OGD condition and to 1.76 ([1.66, 1.84], $p = 0.051$) in the 1.5 h OGD condition (Fig. 4 *B*).

Please cite this article in press as: Schimek et al., High-fidelity predictions of diffusion in the brain microenvironment, Biophysical Journal (2024), https://doi.org/10.1016/j.bpj.2024.10.005

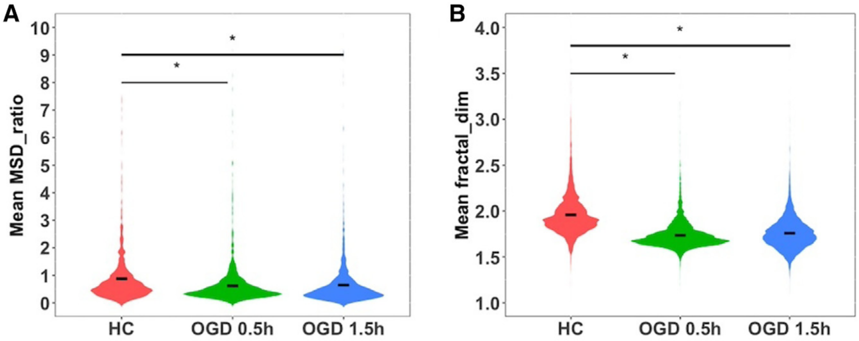

FIGURE 4 Distributions of statistically significant features from cortex when accounting for fixed effects. (*A*) Violin plots showing the distributions of the mean MSD_ratio feature for HC, OGD 0.5 h, and OGD 1.5 h conditions in the cortex. (*B*) Violin plots showing the distribution of the mean fractal_dim feature for HC, OGD 0.5 h, and OGD 1.5 h conditions in the cortex. Statistical significance compared with HC (*$p < 0.05$).

For the striatum data, mean straightness and mean efficiency were statistically significant for both treatment groups, while mean fractal_dim and mean alpha were only significant for the 1.5 h OGD treatment condition. The mean of the mean alpha feature was 0.76 for the HC, increasing to 0.9 (95% confidence interval of [0.863, 0.937], $p = 0.055$) in the 0.5 h OGD condition and to 0.94 ([0.889, 0.963], $p = 0.036$) in the 1.5 h OGD condition (Fig. 5 *A*). Mean straightness had a mean of 0.09 in the HC, which increased to 0.19 ([0.164, 0.208], $p = 0.021$) in the 0.5 h OGD condition and was 0.21 ([0.184, 0.229], $p = 0.011$) in the 1.5 h OGD condition (Fig. 5 *B*). The mean of the mean efficiency feature was 0.22 in the HC, 0.78 ([0.661, 0.877], $p = 0.012$) in the 0.5 h OGD condition, and 0.89 ([0.743, 0.959], $p = 0.008$) in the 1.5 h OGD condition (Fig. 5 *C*). For mean fractal_dim the mean was 2.46 in the HC, which decreased to 1.78 ([1.61, 2.02], $p = 0.058$) in the 0.5 h OGD condition and further to 1.71 ([1.57, 1.98], $p = 0.046$) in the 1.5 h OGD condition (Fig. 5 *D*).

XGBoost and SHAP predict healthy and OGD-treated data and determine key features

To ensure that slice effects of nonstatistically significant features did not impact the XGBoost model predictions, all trajectories from one slice for each condition were held out as the test set during model training and the remaining data were used for training. Model accuracy was then calculated based on predictions on the held-out data. Fifty models were trained for each region, with the mean accuracy on the cortex data being 58.70 ± 0.06% and the mean accuracy on the striatum data being 66.46 ± 0.05%. By training an XGBoost model on the MPT data and using SHAP values to determine feature importance, we aimed to determine whether the model could accurately distinguish between nanoparticles diffusing in disease compared with healthy conditions and find features that could be further investigated to understand changes to the ECM with disease onset.

XGBoost models were able to accurately classify trajectories from healthy brain slices in both the cortex (Fig. 6 *A*) and striatum (Fig. 6 *C*), rarely predicting trajectories from healthy slices as from an injured slice. While the accuracy of the XGBoost models did decrease when making predictions on the two injury conditions in both the cortex and striatum, the predictive accuracy for each class was still well above random guessing. In addition, the mistakes were primarily the model predicting one injury condition as the other injury condition, rather than incorrectly classifying a trajectory from an injury condition as one from a healthy condition. These results demonstrate that an XGBoost model can accurately determine the trends on the data that differentiate trajectories moving in healthy brain slices compared with ones treated with OGD and can detect enough differences between the two OGD conditions to predict at an accuracy above random guessing.

Calculating SHAP values for each feature reveals regional differences in what features most contribute to an XGBoost model's predictions. For the striatum data, the total magnitude of the mean fractal dimension is more than three times greater than the second most important feature (Fig. 6 *D*). While mean fractal dimension was also the top feature for the cortex data set (Fig. 6 *B*), the magnitudes of the top 5 features were much closer compared with the striatum data. These results indicate that changes to the brain microenvironment as a result of OGD treatment are regionally dependent, supporting prior biological characterization of regional diffusion data (39).

SHAP analysis demonstrates region- and treatment-condition-specific changes to diffusion

By further analyzing the top features as determined by SHAP for each condition from each region, it is possible to gain increased insight into how diffusion changes in each unique microenvironment. This approach enables a deeper understanding of how the magnitude of each feature helps distinguish healthy data from OGD-treated data, and differences between each OGD condition.

For the cortex data, a high mean fractal dimension value, high value of mean asymmetry, and high value of mean alpha, were key features used to distinguish between healthy and either of the OGD classes (Fig. 7, *A*–*C*). Mean

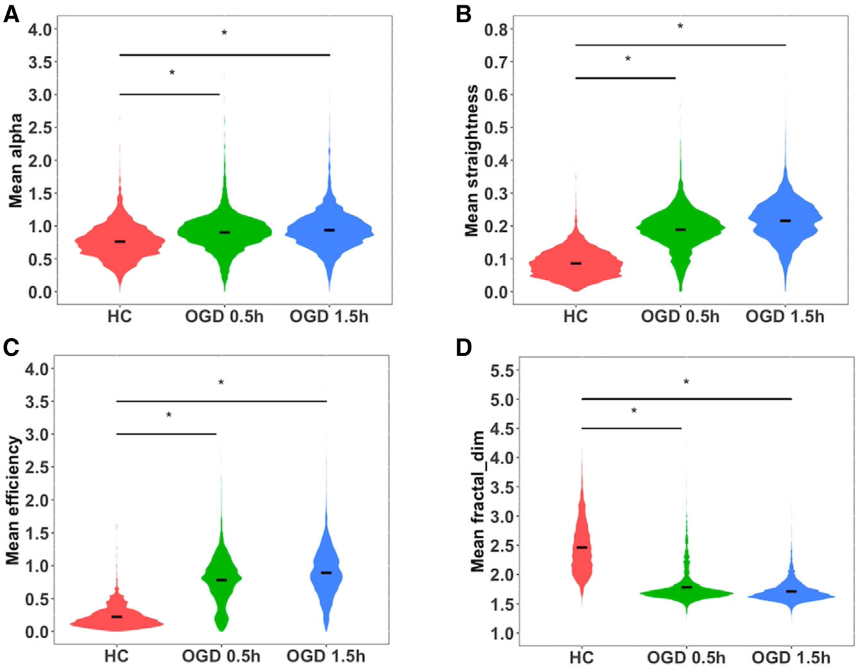

FIGURE 5 Distributions of statistically significant features from striatum when accounting for fixed effects. (*A*) Violin plots showing the distributions of the mean alpha feature for HC, OGD 0.5 h, and OGD 1.5 h conditions in the striatum. (*B*) Violin plots showing the distribution of the mean straightness feature for HC, OGD 0.5 h, and OGD 1.5 h conditions in the striatum. (*C*) Violin plots showing the distributions of the mean efficiency feature for HC, OGD 0.5 h, and OGD 1.5 h conditions in the striatum. (*D*) Violin plots showing the distributions of the mean fractal_dim feature for HC, OGD 0.5 h, and OGD 1.5 h conditions. Statistical significance compared with HC (*$p < 0.05$).

straightness appeared to specifically be useful in differentiating between HC (Fig. 7 *A*) and 1.5 h OGD (Fig. 7 *C*) treatment data. Low values of mean straightness were highly important for HC (Fig. 7 *A*) and high values for 1.5 h treatment (Fig. 7 *C*), but it does not appear as a top 5 feature for 0.5 h OGD treatment (Fig. 7 *B*). Mean Deff1 was the most important feature for the 1.5 h OGD treatment condition, second most important for 0.5 h OGD treatment condition, and also appeared in the top 5 for the HC. Medium to high values of mean Deff1 were indicative of both the 0.5 and 1.5 h OGD treatment conditions (Fig. 7, *B* and *C*), which could help explain why the model struggled to differentiate between the two conditions, while low values of mean Deff1 (Fig. 7 *A*) were associated with the HC condition.

For the striatum data, a high value of mean fractal_dim was also associated with HC compared with low values associated with both OGD conditions (Fig. 7, *D–F*), with mean kurtosis having the same trend. Mean asymmetry1 appeared to help distinguish specifically between HC (Fig. 7 *D*) and 0.5 h OGD (Fig. 7 *E*), where high values were associated with HC and low values associated with 0.5 h OGD data. To further distinguish between HC and 1.5 h OGD data, the model found the mean efficiency to be important, with low values associated with HC (Fig. 7 *D*) and average to high values being associated with 1.5 h OGD (Fig. 7 *F*). Mean Deff1 and mean trappedness were in the top 5 features for both OGD conditions (Fig. 7, *E* and *F*) but not the HC, indicating that these features may indicate an exposure time difference in the response to OGD treatment.

Notably, feature distributions of the top predictors in the SHAP plots show that many predictors have nonlinear relationship with the outcome being predicted (Fig. 7). For example, when predicting HC in the cortex, SHAP values for mean Deff1 are near zero when mean Deff1 is high, but non-zero (both negative and positive) SHAP values are seen when mean Deff1 is low. This is one example of how SHAP analyses allow for better visualization of complex nonlinear relationships that exist between the predictors and the outcome variables.

Overall, these results align with the distributions of the features used (Figs. 4 and 5), highlighting that the XGBoost model is correctly detecting the trends that exist within the data. While this is unsurprising, it is important to confirm that the XGBoost model is picking up on trends in the data known to be present. More importantly, these results demonstrate that SHAP values can be used to go further than the trends shown by the feature distributions and find subsets of statistical features of diffusion, which may be indicative of different responses in brain tissue due to increased OGD exposure time, or due to how different regions respond to OGD. While the results do not directly reveal how the tissue has changed due to OGD treatment, these results highlight aspects of diffusion that could be probed with future experiments.

DISCUSSION

Determining changes to the brain microenvironment in models of disease or injury is critical for the characterization of ECS pathology. While diffusion has been shown to

Please cite this article in press as: Schimek et al., High-fidelity predictions of diffusion in the brain microenvironment, Biophysical Journal (2024), https://doi.org/10.1016/j.bpj.2024.10.005

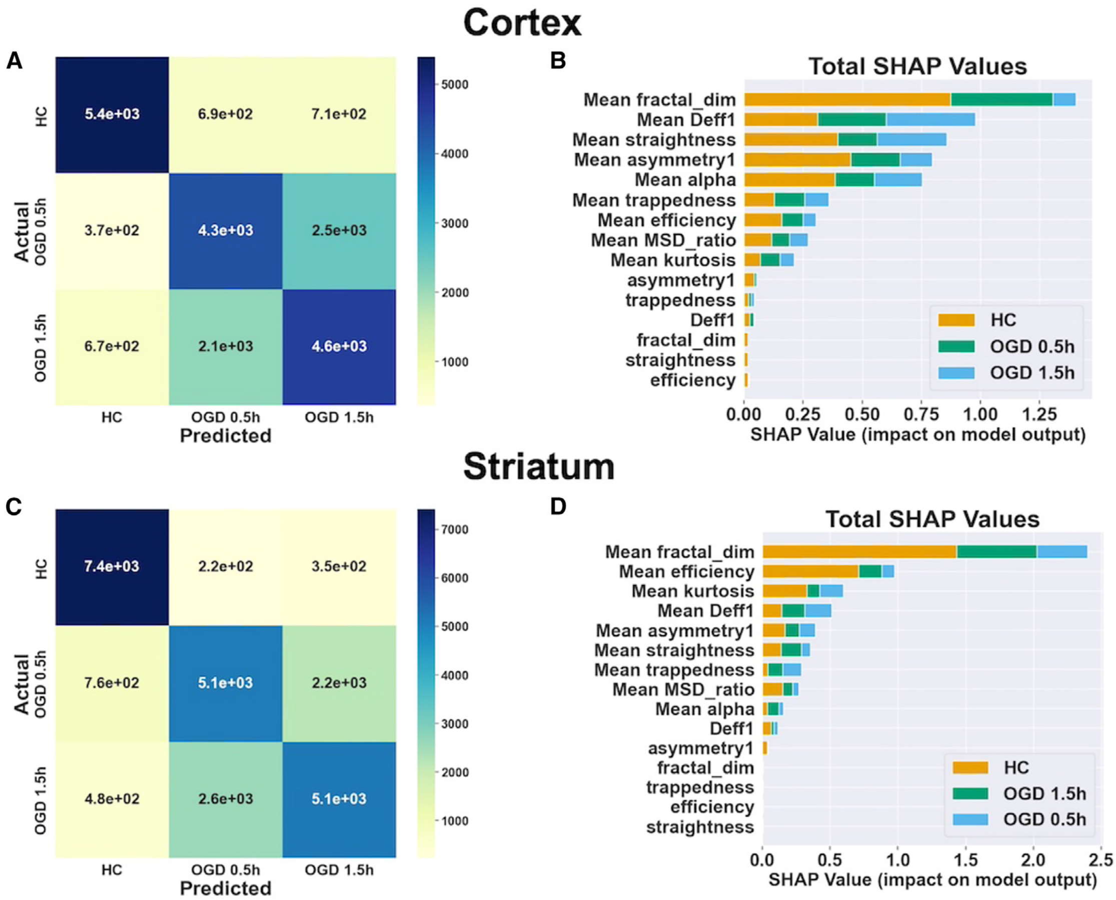

FIGURE 6 Confusion matrices and feature importance values for disease progression predictions. (*A*) XGBoost predictions of 0.5 h OGD, 1.5 h OGD, and nontreated brain slices in the cortex. (*B*) SHAP feature importance values of 0.5 h OGD, 1.5 h OGD, and nontreated brain slices in the cortex. (*C*) XGBoost predictions of 0.5 h OGD, 1.5 h OGD, and nontreated brain slices in the cortex. (*D*) SHAP feature importance values for 0.5 h OGD, 1.5 h OGD, and nontreated brain slices in the cortex.

change due to injury (20,28,30,66,67), studies have focused on bulk changes to diffusion and changes to pore size (40,64). To increase the depth at which changes to diffusion can be analyzed in injury states, we aimed to build a ML pipeline to predict between heathy and injury states and to investigate region and exposure time-specific changes to statistical features of diffusion. To ensure the validity of ML predictions, we first used a pipeline to make predictions under three conditions: biological age, brain region, and enzymatic degradation of ECM components. Because injury across groups is typically measured with traditional statistical approaches, we used linear effects models to compare MPT features across OGD conditions. This approach additionally presents a novel and robust approach to control for correlation between related MPT trajectories when analyzing MPT data. We then show that the ML pipeline predicts between healthy and OGD conditions with good accuracy and helps identify nonlinear relationships and predictors that traditional linear statistics cannot.

The consistency of the ML pipeline described in this paper across multiple data sets demonstrates the feasibility of applying a ML approach to MPT studies for pattern identification in the data that may be informative of biological underpinnings. The application of the Y-scrambling method shows that the technique can properly ensure that the accuracy of the supervised learning models is indeed caused by the model uncovering patterns in the data. The random-guess accuracy and low SHAP values of the XGBoost model trained on Y-scrambled age data further indicate that there are clear differences in diffusion between the P14, P35, and P70 microenvironments that the model can detect. Studies looking at changes in diffusion during the neurodevelopmental process in rats has shown that the ECS volume fraction decreases with age (26). In this study, a large decrease in volume fraction between postnatal days 10 and 21 was observed, but not between P21 and adults aged 90–120 days. Since some of the most important features for the age data set are mean boundedness, mean trappedness, and mean straightness, which relate to the confinement of the nanoparticle trajectory, the model may be picking up changes in nanoparticle diffusion related to in ECS volume fraction between P14, which would have a

Please cite this article in press as: Schimek et al., High-fidelity predictions of diffusion in the brain microenvironment, Biophysical Journal (2024), https://doi.org/10.1016/j.bpj.2024.10.005

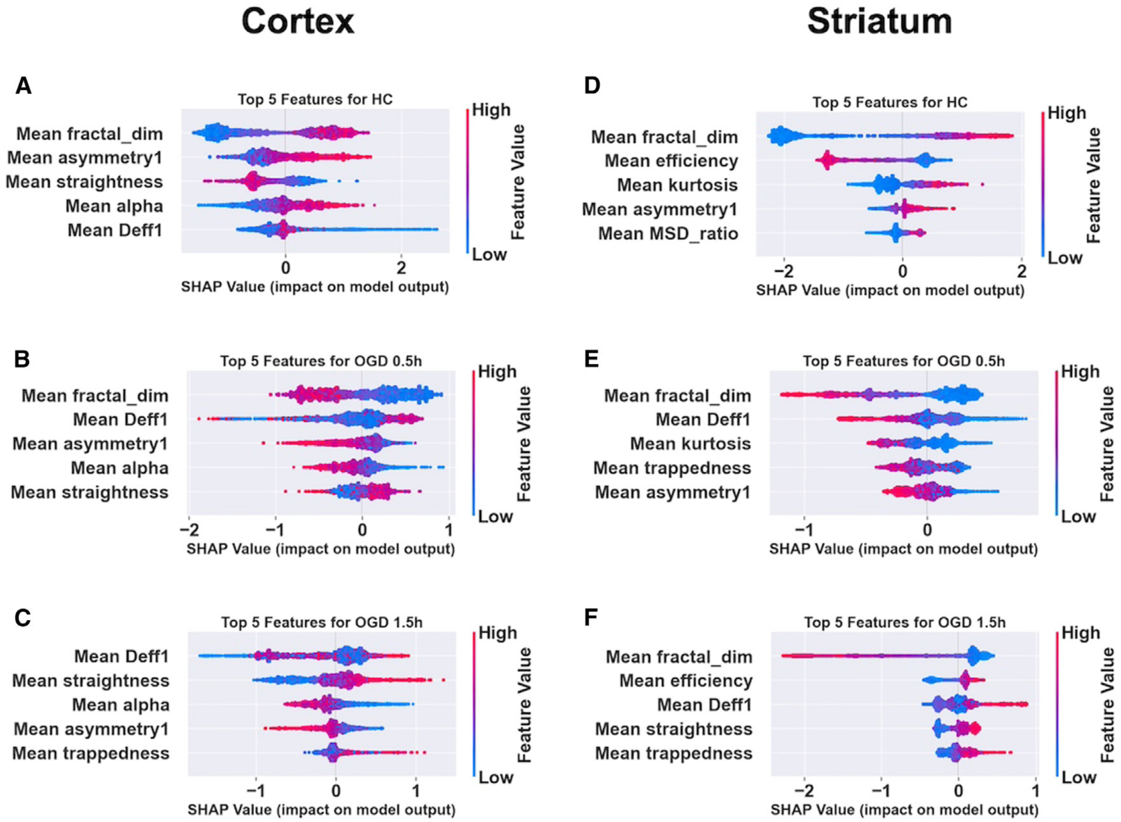

FIGURE 7 SHAP analysis of XGBoost models for each data set shows that mode of injury can be differentiated by unique subsets of trajectory features. Top 5 features determined by SHAP for the cortex for (*A*) HC, (*B*) 0.5 h OGD treatment, and (*C*) 1.5 h OGD treatment. (*D*) Top 5 features determined in the striatum by SHAP for (*D*) HC, (*E*) 0.5 h OGD treatment, and (*F*) 1.5 h OGD treatment.

relatively large volume fraction, and P70, which would have a smaller volume fraction.

Regional volume in the OWH slices used in these studies and more limited data sampling may also be a contributing factor to distinguishing between different brain regions. In this study, 10 videos were recorded and quantified from both the striatum and cortex, but only 6 were collected from each of the hippocampus, basal ganglia, and thalamus. As a result, highlighted by the output of the Y-scrambled model, the data collected from those three regions may have provided enough of a difference in feature values for a model to separate one of the classes from the striatum and cortex, but not enough to differentiate between the three regions that had lower data sampling. Future experimental work could increase video collection in the regions that contain the least number of particles tracked for a more even sample size across brain regions, or account for subregions within the specified brain regions.

That each age or region class had a unique subset of important features determined by SHAP demonstrates that applying explainable ML techniques to SHAP values can elucidate structural information, as it aligned with established knowledge of perineuronal net (PNN) development during aging (68,69). These results confirm that this method detects known differences in ECM structure. Key important features other than those related to diffusion are also likely to pick up differences in the ECM other than PNNs. McKenna et al. suggested that the variance of composition of ECM proteins across development (70,71) could play a role in changing ECM viscosity and obstruction of nanoparticle motion. In addition to effecting features relating to diffusion, these changes could also impact important geometric features relating to nanoparticle travel distance and motion within a confined space (43). Regional differences in diffusion align with results from MRI data in rodents, where diffusivity is different across brain regions in rats (72) and mice (73). Analysis of MRI data from cortex and striatum in adolescent rats showed differences in four measure of diffusivity—T2, mean, axial, and radial—as well as differences in volume and myelination (72). In addition, studies have shown regional differences in microglia populations (74) and brain capillary density (75). Altogether, these differences would alter the space and local structure of the microenvironment through which nanoparticles diffuse for each region, which could cause differences in geometric features that relate to the space taken up by the trajectory, such as mean fractal dimension and mean kurtosis (44).

Please cite this article in press as: Schimek et al., High-fidelity predictions of diffusion in the brain microenvironment, Biophysical Journal (2024), https://doi.org/10.1016/j.bpj.2024.10.005

For the enzyme treatment data set, each enzyme may have different mechanisms of action but degrade the same components of the ECM. When brain slices are treated with ChABC, the effective diffusion coefficient has been shown to increase; however, the degree of degradation may not be sufficient enough for a ML model to detect differences in microstructural changes. The loss of PNNs due to ChABC treatment may also result in neuronal cell death, an inflammatory response, and activation of cells such as microglia (76), which could alter the ECS and ECM, mitigating the effects of the loss of ECM structure. ECM degradation may not be severe enough to cause the statistical features to be different for many of the nanoparticle trajectories. We see this highlighted when looking at Y-scrambled model results and the SHAP values, as the best XGBoost model accuracy was only 19% above random guessing, and only one feature (mean Deff1) had a high impact on the model.

Studies of OGD treatment in rodent brain slices have shown clear differences in diffusion between HC and OGD conditions. OGD treatment has shown an increase in the effective diffusion coefficient (39,40), as well as changes to the distribution of diffusion modes and ECM pore sizes (39). As these measurements are all made from the statistical features that are related to the mean-squared displacement that the model is trained with, it is unsurprising that mean Deff1 and mean alpha were important for the cortex data, while mean Deff1 and mean trappedness were used for both OGD conditions in the region data. Unlike the age, region, and treatment data sets, the top SHAP feature for the OGD data set in both regions was not the mean effective diffusion coefficient, but rather the mean fractal dimension feature, which takes a value near 1 for straight trajectories and direction motion, near 2 for random, Brownian diffusion, and 3 for constrained trajectories (43,77). One possible explanation is that changes to the fractal dimension of the trajectories are related to conditions of cytotoxic and oxidative stress. OGD slices have greater cytotoxicity (39), which could lead to less cell density and straighter, less-confined nanoparticle motion in the OGD conditions compared with HC, as well as the age and region data sets.

Regional differences in the brain ECS also seem to play a role in the SHAP analysis of the XGBoost models trained on the OGD data set, as each of the six classes had a unique subset of top features. The difference in the top 5 features between the cortex and striatum for both the 0.5 h OGD condition and the 1.5 h OGD condition suggests that XGBoost models are able to detect regional differences in the ECS environment after OGD exposure. Regional differences in features due to OGD exposure align with regional differences of diffusion parameters in the ECS due to hypoxia, namely volume fraction and tortuosity. Volume fraction refers to the percentage of volume of the brain ECS relative to the volume of the entire tissue, while tortuosity measures the degree of hindrance to diffusion in tissue relative to free medium. In the striatum of adult rats, volume fraction has been shown to decrease due to hypoxia with no change to tortuosity (28), while in the cortex volume fraction has been shown to decrease while tortuosity increases (66,67).

A benefit of training XGBoost models on MPT data from OWH slices is that other modalities of data are collected, allowing for comparison of changes to the extracellular environment and other impacts of disease. OGD is known to effect microglia populations (78), and cellular-extracellular interactions may influence the environment through which nanoparticles are diffusing. Previous work showed that the morphology of microglia became more heterogeneous compared with a healthy microglia population, as well as a reduced overall number of microglia (39). A study looking at changes to microglia over the course of 48 h shows changes to morphological parameters such as perimeter, area, circularity, and aspect ratio differed from normal conditions (64). The reduced density of microglia due to OGD and change in shape in response to disease could explain the high values of features such as mean straightness in the cortex and mean efficiency in the striatum were important to OGD conditions, where reduced cellular density would reduce hindrance to diffusing nanoparticles. Microglia may also contribute to differences in important features across regions. A study in ex vivo ferret brain treated with OGD found region-dependent changes to microglia morphology features such as perimeter, circularity, and area across the cortex, corpus callosum, hippocampus, basal ganglia, thalamus, and subcortical matter (79). While it is unclear whether microglia impact the SHAP features in this study, future studies may collect particle tracking data and microglia or other cell morphology data from the same OWH slice to better understand the relationship between nanoparticle diffusion and cellular changes under pathological conditions.

The importance of locally averaged features across all four data sets indicate that local averaging is a significant contributor to model performance and can be beneficial to include in future MPT ML work. It may also highlight that it is not individual trajectories that provide robust information to a data set, but the distribution and diversity of nanoparticle motion within a given subspace. Research into the structure of the brain ECS has shown there to be void spaces connected via tortuous channels (5,32,80) and reservoirs of space next to cells (81). As noted in McKenna et al. (41), it is likely that neighboring nanoparticles diffusing in these voids will be experiencing nearly identical environments and have similar diffusive behavior, while trajectories moving in an ECS channel of varying width will have different diffusive behavior. The ECS is also known to vary across age, brain region, and disease (5,32). Locally averaged features as the top feature across all four data sets

Please cite this article in press as: Schimek et al., High-fidelity predictions of diffusion in the brain microenvironment, Biophysical Journal (2024), https://doi.org/10.1016/j.bpj.2024.10.005

supports the idea that these features are capturing changes in the motion of neighboring nanoparticles resulting from structural differences in the ECM.

One limitation in this study is our identification of classes for each data set that are not able to be differentiated with high accuracy with the chosen ML models. Past research has shown that a deep learning approach can be used for nanoparticle trajectory classification tasks by applying a convolutional neural network to the raw trajectory data (44,82). For each of these data sets, future work can investigate whether or not a deep learning approach on raw trajectory data, as opposed to the statistical features used in this study, can improve the accuracy of predictions on classes with which these current methods struggle. Synthetic data can also be generated using a generative adversarial network deep learning approach, which has been shown to improve convolutional neural network accuracy in medical classification tasks (83). The mechanism relating locally average features to specific structural and microenvironmental changes also remains unclear. Future work could combine MPT with live-slice staining and imaging to determine how cellular- and protein-level changes influence nanoparticle diffusion, both at the individual trajectory level and over locally averaged domains. ML integration into MPT data analysis could also be applied in a nonbrain context, such as making predictions on nanoparticles moving in other biological environments such as the mucosal membrane (84), or for tracking the diffusion of viruses and viral vectors (85). While our analysis indicates that XGBoost can be used to predict between healthy and disease states, we are unable to directly relate differences in the most important features between healthy slices and OGD slices directly to the known changes due to OGD exposure. Future work will incorporate an increased amount of data relating to the disease condition to find correlations between features extracted from MPT experiments and macroscopic changes to the ECS.

CONCLUSION

We outline a methodology to apply data science and ML tools to MPT data to probe underlying biological changes using four distinct experimental data sets. While MPT has long been a technique used to understand complex biological environments, our methodology increases the insights extracted from a given MPT data set. Specifically, we validate the use of supervised learning and feature importance techniques by detecting microenvironmental changes in the brain ECS that align with previous characterizations of age and regional differences in tissue. We then demonstrate that XGBoost and SHAP can be applied to MPT data collected in models of disease to detect specific changes to the ECS microstructure based on treatment condition, treatment exposure time, and regional responses to injury.

DATA AND CODE AVAILABILITY

The data used for this research can be found in the diff_predictor GitHub repository: https://github.com/Nance-Lab/diff_predictor. The source code used for this research can be found in the diff_predictor GitHub repository: https://github.com/Nance-Lab/diff_predictor.

ACKNOWLEDGMENTS

This work was supported by the National Institute of General Medical Sciences grant no. R35GM124677, the National Science Foundation grant no. HDR1934292, and the Azure Cloud Computing Credits for Research and Teaching award no. MS-AZR-0143P.

AUTHOR CONTRIBUTIONS

N.S., D.A.C.B., T.R.W., and E.N. wrote the main manuscript text. M.M. generated the experimental data. N.S. and A.T. carried out all ML and data analyses. D.A.C.B. and E.N. supervised the project and acquired the funding support. N.S. prepared all figures. T.R.W. guided the statistical analysis, including application and interpretation of the mixed linear models. All authors edited and revised the original manuscript. N.S., T.R.W., and E.N. carried out revisions in response to peer review. All authors reviewed the final manuscript.

DECLARATION OF INTERESTS

The authors declare no competing interests.

SUPPORTING MATERIAL

Supporting material can be found online at https://doi.org/10.1016/j.bpj.2024.10.005.

REFERENCES

1. Long, K. R., and W. B. Huttner. 2019. How the extracellular matrix shapes neural development. *Open Biol.* 9:180216.
2. Barros, C. S., S. J. Franco, and U. Müller. 2011. Extracellular matrix: functions in the nervous system. *Cold Spring Harbor Perspect. Biol.* 3:a005108.
3. Suttkus, A., M. Morawski, and T. Arendt. 2016. Protective Properties of Neural Extracellular Matrix. *Mol. Neurobiol.* 53:73–82.
4. Kamali-Zare, P., and C. Nicholson. 2013. Brain extracellular space: geometry, matrix and physiological importance. *Basic Clin. Neurosci.* 4:282–286.
5. Syková, E., and C. Nicholson. 2008. Diffusion in Brain Extracellular Space. *Physiol. Rev.* 88:1277–1340.
6. Ruoslahti, E. 1996. Brain extracellular matrix. *Glycobiology.* 6:489–492.
7. Jenkins, H. G., and H. S. Bachelard. 1988. Developmental and age-related changes in rat brain glycosaminoglycans. *J. Neurochem.* 51:1634–1640.
8. Novak, U., and A. H. Kaye. 2000. Extracellular matrix and the brain: components and function. *J. Clin. Neurosci.* 7:280–290.
9. Yamaguchi, Y. 2000. Lecticans: organizers of the brain extracellular matrix. *Cell. Mol. Life Sci.* 57:276–289.
10. Margolis, R. K., and R. U. Margolis. 1993. Nervous tissue proteoglycans. *Experientia.* 49:429–446.
11. Fawcett, J. W., M. Fyhn, …, B. A. Sorg. 2022. The extracellular matrix and perineuronal nets in memory. *Mol. Psychiatr.* 27:3192–3203.

12. Brückner, G., W. Härtig, …, K. Brauer. 1996. Extracellular matrix organization in various regions of rat brain grey matter. *J. Neurocytol.* 25:333–346.
13. Dauth, S., T. Grevesse, …, K. K. Parker. 2016. Extracellular matrix protein expression is brain region dependent. *J. Comp. Neurol.* 524:1309–1336.
14. Lyall, A. E., O. Pasternak, …, P. R. Szeszko. 2018. Greater extracellular free-water in first-episode psychosis predicts better neurocognitive functioning. *Mol. Psychiatr.* 23:701–707.
15. Seitz-Holland, J., Y. Alemán-Gómez, …, D. Dwir. 2024. Matrix metalloproteinase 9 (MMP-9) activity, hippocampal extracellular free water, and cognitive deficits are associated with each other in early phase psychosis. *Neuropsychopharmacology.* 49:1140–1150.
16. Tureckova, J., M. Kamenicka, …, M. Anderova. 2021. Compromised Astrocyte Swelling/Volume Regulation in the Hippocampus of the Triple Transgenic Mouse Model of Alzheimer's Disease. *Front. Aging Neurosci.* 13:783120.
17. Shen, T., Y. Yue, …, H. Y. Lai. 2022. Diffusion along perivascular spaces as marker for impairment of glymphatic system in Parkinson's disease. *NPJ Parkinsons Dis.* 8:174.
18. McKnight, C. D., P. Trujillo, …, D. O. Claassen. 2021. Diffusion along perivascular spaces reveals evidence supportive of glymphatic function impairment in Parkinson disease. *Parkinsonism Relat. Disord.* 89:98–104.
19. Ma, X., S. Li, …, W. Su. 2021. Diffusion Tensor Imaging Along the Perivascular Space Index in Different Stages of Parkinson's Disease. *Front. Aging Neurosci.* 13:773951.
20. Syková, E., I. Vořı́šek, …, J. Bureš. 2005. Changes in extracellular space size and geometry in APP23 transgenic mice: A model of Alzheimer's disease. *Proc. Natl. Acad. Sci. USA.* 102:479–484.
21. Sun, Y., S. Xu, …, Q. Yang. 2021. Role of the Extracellular Matrix in Alzheimer's Disease. *Front. Aging Neurosci.* 13
22. George, N., and H. M. Geller. 2018. Extracellular matrix and traumatic brain injury. *J. Neurosci. Res.* 96:573–588.
23. Griffiths, D. R., T. M. Jenkins, …, J. Lifshitz. 2020. Extracellular matrix proteins are time-dependent and regional-specific markers in experimental diffuse brain injury. *Brain Behav.* 10:e01767.
24. Nicholson, C., and E. Syková. 1998. Extracellular space structure revealed by diffusion analysis. *Trends Neurosci.* 21:207–215.
25. Syková, E. 2004. Extrasynaptic volume transmission and diffusion parameters of the extracellular space. *Neuroscience.* 129:861–876.
26. Lehmenkühler, A., E. Syková, …, C. Nicholson. 1993. Extracellular space parameters in the rat neocortex and subcortical white matter during postnatal development determined by diffusion analysis. *Neuroscience.* 55:339–351.
27. Kume-Kick, J., T. Mazel, …, C. Nicholson. 2002. Independence of extracellular tortuosity and volume fraction during osmotic challenge in rat neocortex. *J. Physiol.* 542:515–527.
28. Rice, M. E., and C. Nicholson. 1991. Diffusion characteristics and extracellular volume fraction during normoxia and hypoxia in slices of rat neostriatum. *J. Neurophysiol.* 65:264–272.
29. Syková, E., J. Svoboda, …, H. Lassmann. 1996. X-irradiation-induced changes in the diffusion parameters of the developing rat brain. *Neuroscience.* 70:597–612.
30. Hrabětová, S., J. Hrabe, and C. Nicholson. 2003. Dead-Space Microdomains Hinder Extracellular Diffusion in Rat Neocortex during Ischemia. *J. Neurosci.* 23:8351.
31. Hrabetová, S., and C. Nicholson. 2004. Contribution of dead-space microdomains to tortuosity of brain extracellular space. *Neurochem. Int.* 45:467–477.
32. Thorne, R. G., and C. Nicholson. 2006. In vivo diffusion analysis with quantum dots and dextrans predicts the width of brain extracellular space. *Proc. Natl. Acad. Sci. USA.* 103:5567–5572.
33. Nance, E. A., G. F. Woodworth, …, J. Hanes. 2012. A dense poly(ethylene glycol) coating improves penetration of large polymeric nanoparticles within brain tissue. *Sci. Transl. Med.* 4:149ra119.
34. Paviolo, C., F. N. Soria, …, L. Cognet. 2020. Nanoscale exploration of the extracellular space in the live brain by combining single carbon nanotube tracking and super-resolution imaging analysis. *Methods.* 174:91–99.
35. Antoine, G., J. A. V. Godin, …, L. Groc. 2017. Single-nanotube tracking reveals the nanoscale organization of the extracellular space in the live brain. *Nat. Nanotechnol.* 12:238–243.
36. Manzo, C., and M. F. Garcia-Parajo. 2015. A review of progress in single particle tracking: from methods to biophysical insights. *Rep. Prog. Phys.* 78:124601.
37. Paviolo, C., and L. Cognet. 2021. Near-infrared nanoscopy with carbon-based nanoparticles for the exploration of the brain extracellular space. *Neurobiol. Dis.* 153:105328.
38. Soria, F. N., C. Paviolo, …, E. Bezard. 2020. Synucleinopathy alters nanoscale organization and diffusion in the brain extracellular space through hyaluronan remodeling. *Nat. Commun.* 11:3440.
39. Joseph, A., R. Liao, …, E. Nance. 2020. Nanoparticle-microglial interaction in the ischemic brain is modulated by injury duration and treatment. *Bioeng. Transl. Med.* 5:e10175.
40. McKenna, M., J. R. Filteau, …, E. Nance. 2022. Organotypic whole hemisphere brain slice models to study the effects of donor age and oxygen-glucose-deprivation on the extracellular properties of cortical and striatal tissue. *J. Biol. Eng.* 16:14.
41. McKenna, M., D. Shackelford, …, E. Nance. 2021. Multiple Particle Tracking Detects Changes in Brain Extracellular Matrix and Predicts Neurodevelopmental Age. *ACS Nano.* 15:8559–8573.
42. Pinholt, H. D., S. S. R. Bohr, …, N. S. Hatzakis. 2021. Single-particle diffusional fingerprinting: A machine-learning framework for quantitative analysis of heterogeneous diffusion. *Proc. Natl. Acad. Sci. USA.* 118:e2104624118.
43. Wagner, T., A. Kroll, …, M. Wiemann. 2017. Classification and Segmentation of Nanoparticle Diffusion Trajectories in Cellular Micro Environments. *PLoS One.* 12:e0170165.
44. Kowalek, P., H. Loch-Olszewska, and J. Szwabiński. 2019. Classification of diffusion modes in single-particle tracking data: Feature-based versus deep-learning approach. *Phys. Rev. E.* 100:032410.
45. Muñoz-Gil, G., M. A. Garcia-March, …, M. Lewenstein. 2020. Single trajectory characterization via machine learning. *New J. Phys.* 22:013010.
46. Maris, J. J. E., F. T. Rabouw, …, F. Meirer. 2022. Classification-based motion analysis of single-molecule trajectories using DiffusionLab. *Sci. Rep.* 12:9595.
47. Gentili, A., and G. Volpe. 2021. Characterization of anomalous diffusion classical statistics powered by deep learning (CONDOR). *J. Phys. Math. Theor.* 54:314003.
48. Al-Hada, E. A., X. Tang, and W. Deng. 2022. Classification of stochastic processes by convolutional neural networks. *J. Phys. Math. Theor.* 55:274006.
49. Hatzakis, N. S., J. Kaestel-Hansen, …, T. Kirchhausen. 2024. Deep learning assisted single particle tracking for automated correlation between diffusion and function. *Res. Square.* rs.3:rs-3716053.
50. Gajowczyk, M., and J. Szwabiński. 2021. Detection of Anomalous Diffusion with Deep Residual Networks. *Entropy.* 23:649.
51. Garibo i Orts, Ò., M. A. Garcia-March, and J. A. Conejero. 2021. Efficient recurrent neural network methods for anomalously diffusing single particle short and noisy trajectories. *J. Phys. Math. Theor.* 54:504002.
52. Zhang, Y., F. Ge, …, Y. He. 2023. Extract latent features of single-particle trajectories with historical experience learning. *Biophys. J.* 122:4451–4466.
53. Requena, B., S. Masó-Orriols, …, G. Muñoz-Gil. 2023. Inferring pointwise diffusion properties of single trajectories with deep learning. *Biophys. J.* 122:4360–4369.
54. Seckler, H., J. Szwabiński, and R. Metzler. 2023. Machine-Learning Solutions for the Analysis of Single-Particle Diffusion Trajectories. *J. Phys. Chem. Lett.* 14:7910–7923.

Please cite this article in press as: Schimek et al., High-fidelity predictions of diffusion in the brain microenvironment, Biophysical Journal (2024), https://doi.org/10.1016/j.bpj.2024.10.005

55. Kaler, L., K. Joyner, and G. A. Duncan. 2022. Machine learning-informed predictions of nanoparticle mobility and fate in the mucus barrier. *APL Bioeng.* 6:026103.
56. Curtis, C., M. McKenna, …, E. Nance. 2019. Predicting in situ nanoparticle behavior using multiple particle tracking and artificial neural networks. *Nanoscale.* 11:22515–22530.
57. Stoica, B. A., and A. I. Faden. 2010. Cell Death Mechanisms and Modulation in Traumatic Brain Injury. *Neurotherapeutics.* 7:3–12.
58. Nance, E. 2017. Brain-Penetrating Nanoparticles for Analysis of the Brain Microenvironment. *Methods Mol. Biol.* 1570:91–104.
59. Bates, D., M. Mächler, …, S. Walker. 2015. Fitting Linear Mixed-Effects Models Using lme4. *J. Stat. Softw.* 67:1–48.
60. Team, R.C.. 2020. RA language and environment for statistical computing. R Foundation for Statistical. Computing.
61. Chen, T., and C. Guestrin. 2016. XGBoost: A Scalable Tree Boosting System. *In* Proceedings of the 22nd ACM SIGKDD International Conference on Knowledge Discovery and Data Mining. Association for Computing Machinery, San Francisco, California, USA, pp. 785–794.
62. Hastie, T., R. Tibishirani, and J. Friedman. 2009. The Elements of Statistical Learning. *In* Springer Series in Statistics. P. Bühlmann…, eds Springer.
63. Lundberg, S. M., G. Erion, …, S. I. Lee. 2020. From local explanations to global understanding with explainable AI for trees. *Nat. Mach. Intell.* 2:56–67.
64. Nguyen, N. P., H. Helmbrecht, …, E. Nance. 2022. Brain Tissue-Derived Extracellular Vesicle Mediated Therapy in the Neonatal Ischemic Brain. *Int. J. Mol. Sci.* 23:620.
65. Curtis, C., A. Rokem, and E. Nance. 2019. diff_classifier: Parallelization of multi-particle tracking video analyses 4:989.
66. Zoremba, N., A. Homola, …, E. Syková. 2007. Brain metabolism and extracellular space diffusion parameters during and after transient global hypoxia in the rat cortex. *Exp. Neurol.* 203:34–41.
67. Homola, A., N. Zoremba, …, E. Syková. 2006. Changes in diffusion parameters, energy-related metabolites and glutamate in the rat cortex after transient hypoxia/ischemia. *Neurosci. Lett.* 404:137–142.
68. Lensjø, K. K., A. C. Christensen, …, T. Hafting. 2017. Differential Expression and Cell-Type Specificity of Perineuronal Nets in Hippocampus, Medial Entorhinal Cortex, and Visual Cortex Examined in the Rat and Mouse. *eneuro.* 4:ENEURO.0379-16.2017.
69. Baker, K. D., A. R. Gray, and R. Richardson. 2017. The development of perineuronal nets around parvalbumin gabaergic neurons in the medial prefrontal cortex and basolateral amygdala of rats. *Behav. Neurosci.* 131:289–303.
70. Gao, R., M. Wang, …, L. Yuan. 2018. Spatiotemporal expression patterns of chondroitin sulfate proteoglycan mRNAs in the developing rat brain. *Neuroreport.* 29:517–523.
71. Margolis, R. U., R. K. Margolis, …, C. Preti. 1975. Glycosaminoglycans of brain during development. *Biochemistry.* 14:85–88.
72. Mengler, L., A. Khmelinskii, …, M. Hoehn. 2014. Brain maturation of the adolescent rat cortex and striatum: Changes in volume and myelination. *Neuroimage.* 84:35–44.
73. Budin, F., M. Hoogstoel, …, I. Oguz. 2013. Fully automated rodent brain MR image processing pipeline on a Midas server: from acquired images to region-based statistics. *Front. Neuroinf.* 7:15.
74. Furube, E., S. Kawai, …, S. Miyata. 2018. Brain Region-dependent Heterogeneity and Dose-dependent Difference in Transient Microglia Population Increase during Lipopolysaccharide-induced Inflammation. *Sci. Rep.* 8:2203.
75. Cavaglia, M., S. M. Dombrowski, …, D. Janigro. 2001. Regional variation in brain capillary density and vascular response to ischemia. *Brain Res.* 910:81–93.
76. Bonneh-Barkay, D., and C. A. Wiley. 2009. Brain Extracellular Matrix in Neurodegeneration. *Brain Pathol.* 19:573–585.
77. Katz, M. J., and E. B. George. 1985. Fractals and the analysis of growth paths. *Bull. Math. Biol.* 47:273–286.
78. Girard, S., D. Brough, …, S. M. Allan. 2013. Microglia and macrophages differentially modulate cell death after brain injury caused by oxygen-glucose deprivation in organotypic brain slices. *Glia.* 61:813–824.
79. Wood, T. R., K. Hildahl, …, E. Nance. 2022. A ferret brain slice model of oxygen–glucose deprivation captures regional responses to perinatal injury and treatment associated with specific microglial phenotypes. *Bioeng. Transl. Med.* 7:e10265.
80. Van Harreveld, A., J. Crowell, and S. K. Malhotra. 1965. A STUDY OF EXTRACELLULAR SPACE IN CENTRAL NERVOUS TISSUE BY FREEZE-SUBSTITUTION. *J. Cell Biol.* 25:117–137.
81. Hrabetova, S., L. Cognet, …, U. V. Nägerl. 2018. Unveiling the Extracellular Space of the Brain: From Super-resolved Microstructure to In Vivo Function. *J. Neurosci.* 38:9355–9363.
82. Granik, N., L. E. Weiss, …, Y. Shechtman. 2019. Single-Particle Diffusion Characterization by Deep Learning. *Biophys. J.* 117:185–192.
83. Chen, R. J., M. Y. Lu, …, F. Mahmood. 2021. Synthetic data in machine learning for medicine and healthcare. *Nat. Biomed. Eng.* 5:493–497.
84. Schneider, C. S., Q. Xu, …, J. Hanes. 2017. Nanoparticles that do not adhere to mucus provide uniform and long-lasting drug delivery to airways following inhalation. *Sci. Adv.* 3:e1601556.
85. Kaler, L., E. Iverson, …, G. A. Duncan. 2022. Influenza A virus diffusion through mucus gel networks. *Commun. Biol.* 5:249.